

# Ferroelectricity and Crystal Phases in Mixed-Cation Lead Iodide Perovskite Solar Cells

Alexander Deniz Schulz, Max Oliver Schmitt, Moritz Braun, Alexander Colsmann, Manuel Hinterstein, and Holger Röhm\*

After the discovery of ferroelectricity in archetypal methylammonium lead iodide (MAPbI<sub>3</sub>), the discussion arose, if more advanced derivatives thereof are also ferroelectric and to what extent the polar domains mitigate detrimental charge carrier recombination in perovskite solar cells. Herein, the A-site cation methylammonium is gradually substituted with formamidinium and cesium. The domain contrast measured by piezoresponse force microscopy is correlated with the distortion of the crystal structure measured by X-ray diffraction. By Rietveld analysis, a detailed structural model together with texture information is determined, which reveals an intriguing interplay between lead iodide and the perovskite phases. Finally, the bearing of ferroelectric domains in mixed-cation perovskites on the solar cell performance is discussed.

## 1. Introduction

Organic metal halide (OMH) perovskites are a versatile class of materials, not least due to their feature to form solid solutions, which enable the tailoring of properties for light-harvesting solar cells, light-emitting diodes, lasers, and many other applications. The archetypal methylammonium lead iodide (MAPbI<sub>3</sub>) inherits its principal electronic band structure from the orbital configurations of lead on the B-site of the ABX<sub>3</sub> perovskite crystal and iodide on the X-site.<sup>[1]</sup> A unique feature of OMH perovskites is the dipolar molecular cation on the A-site, which has an indirect

influence on the band structure by affecting the bond lengths and the angles of the PbI<sub>6</sub> octahedra. Frost et al. and Liu et al. predicted the formation of ferroelectric domains as a result of the dipole alignment of methylammonium cations and further proposed that these polar domains may spatially separate photogenerated electrons and holes, thus reducing charge carrier recombination losses in solar cells.<sup>[1,2]</sup> Employing optical methods, Sarritzu et al. found Shockley–Read–Hall (SRH) recombination to prevail in electrode-free perovskite layers, but they also noted that, in devices with electrodes, interface recombination can become more prominent than bulk recombination.<sup>[3]</sup> In either case,

spatial separation of charge carriers can reduce the rate of recombination. Using drift-diffusion simulations, Rossi et al. and Sherkar et al. set out to quantify the impact of polar domains on the solar cell performance.<sup>[4,5]</sup> Rossi et al. based their simulation on ferroelectric domain patterns that were measured in MAPbI<sub>3</sub> thin films and gradually tuned the magnitude of polarization to match experimental current density–voltage (*J*–*V*) curves. While Rossi et al. assumed SRH recombination to be the prevailing recombination mechanism, Sherkar et al. assumed predominant bimolecular recombination. According to both reports, the most significant improvement was the enhancement of the fill factor from 69 to 84% (at a polarization strength of  $P = 0.05 \mu\text{C cm}^{-2}$ ) or from 52 to 77% ( $P = 0.4 \mu\text{C cm}^{-2}$ ), respectively. In the report of Rossi et al., this polarization fostered a remarkable improvement in power conversion efficiency (PCE) from 11 to 18.5%.


After first claims of rather randomly shaped ferroelectric domains in small MAPbI<sub>3</sub> grains measured by piezoresponse force microscopy (PFM), Hermes et al. and Röhm et al. identified ordered domains within larger MAPbI<sub>3</sub> grains.<sup>[6–8]</sup> These patterns were interpreted to be of ferroelastic or ferroelectric nature, respectively. The hallmark of ferroelasticity is permanent switching of domains by external mechanical stress as demonstrated by Strelcov et al.<sup>[9]</sup> The hallmark of ferroelectricity is permanent switching of domains by an external electric field, as reported by Röhm et al. after lateral DC poling of MAPbI<sub>3</sub> thin films.<sup>[10]</sup> Notably, common ferroelectric perovskites such as barium titanate and lead zirconate titanate are also ferroelastic.<sup>[11–13]</sup>

Yet, as of today, reports are sparse on both ferroelectric or ferroelastic domains in any of the more advanced mixed-

A. D. Schulz, M. O. Schmitt, A. Colsmann, H. Röhm  
Material Research Center for Energy Systems  
Karlsruhe Institute of Technology (KIT)  
76131 Karlsruhe, Germany  
E-mail: holger.roehm@kit.edu

A. D. Schulz, A. Colsmann, H. Röhm  
Light Technology Institute  
Karlsruhe Institute of Technology (KIT)  
76131 Karlsruhe, Germany

M. Braun, M. Hinterstein  
Institute for Applied Materials – Ceramic Materials and Technologies  
Karlsruhe Institute of Technology (KIT)  
76131 Karlsruhe, Germany

 The ORCID identification number(s) for the author(s) of this article can be found under <https://doi.org/10.1002/solr.202200808>.

© 2022 The Authors. Solar RRL published by Wiley-VCH GmbH. This is an open access article under the terms of the Creative Commons Attribution License, which permits use, distribution and reproduction in any medium, provided the original work is properly cited.

DOI: 10.1002/solr.202200808

cation OMH perovskites, which contain combinations of methylammonium (MA), formamidinium (FA), and cesium on the A-site.<sup>[14–16]</sup> This raises the question whether or not ferroelectricity and ferroelasticity are exclusive features of MAPbI<sub>3</sub> caused by the MA cation. Ferroelectricity requires lowering the unit cell symmetry, and creating a polar axis, spontaneous polarization, and multiple possible polarization orientations.<sup>[17]</sup> By nature, cubic crystals are nonferroelectric, which manifests in the nonexistence of polar cubic point groups. However, in OMH perovskites, the partially disordered organic cations often hamper an unambiguous determination of the crystal phase.<sup>[18–23]</sup> As Stroppa et al. pointed out, the organic cation can have two fundamentally different contributions to the ferroelectricity of MAPbI<sub>3</sub>: the intrinsic electric dipole moment of the rotatable molecular A-site cation as well as the dipole moment arising from the relative positions of the A-site cation and the inorganic framework.<sup>[24]</sup> Employing density functional theory (DFT), they predicted that the contribution of the relative displacement of the MA cation is considerably larger than the contribution of the intrinsic dipole moment, and that hydrogen bonding between MA and iodide drives this displacement. Using single-crystal X-ray diffraction, Breternitz et al. showed experimental evidence of the displacement of iodide out of the a-b plane of the crystal.<sup>[23]</sup> Altogether, tetragonal MAPbI<sub>3</sub> exhibits a distortion of its inorganic framework that is detectable in X-ray diffraction experiments and that can be connected to its ferroelectric properties.

In formamidinium lead iodide (FAPbI<sub>3</sub>), Weller et al. discovered a cubic (PbI<sub>3</sub>)<sup>−</sup> framework with partially disordered FA cations on the A-site.<sup>[25]</sup> FAPbI<sub>3</sub> being cubic can be rationalized by the Goldschmidt tolerance factor, which is closer to 1 than for MAPbI<sub>3</sub>, since FA (size: 253 pm) is significantly larger than MA (size: 217 pm).<sup>[26]</sup> In contrast, the incorporation of a smaller cation like 12-fold coordinated cesium (size: 188 pm) reduces the Goldschmidt tolerance factor and, hence, is expected to introduce further distortion.<sup>[27]</sup> Francisco-López et al. and Weber et al. reported that the gradual replacement of MA by FA in mixed-cation FAMA solid solutions leads to the transition from a tetragonal to a cubic phase between MA concentrations of 90% and 80%.<sup>[28,29]</sup> Thus, we hypothesize a concomitant transition from a ferroelectric to a nonferroelectric phase in this composition regime.

In this work, we gradually replace MA in the well-investigated MAPbI<sub>3</sub> with FA and Cs. We investigate the crystal phases of the samples by X-ray diffraction and study the composition-dependent tetragonal-to-cubic phase transition. We then probe the mixed-cation perovskite thin films for changes in the ferroelectric domain pattern using PFM, which is an atomic force microscopy (AFM) technique. Finally, we incorporate these thin films into solar cells and correlate the crystallographic properties with the photovoltaic performance.

## 2. Results and Discussions

To probe the ferroelectric nature of mixed-cation perovskite thin films, we investigated a series of FA<sub>1−x</sub>MA<sub>x</sub>PbI<sub>3</sub> (FAMA, 0.75 ≤ x ≤ 1) and Cs<sub>0.05</sub>FA<sub>0.95−x</sub>MA<sub>x</sub>PbI<sub>3</sub> (CsFAMA, 0.75 ≤ x ≤ 0.95) thin-film samples. We started our investigation

with an MA concentration of 100%, i.e., MAPbI<sub>3</sub>, for which we optimized the deposition process, as outlined in detail in the experimental section. Then, we gradually replaced MA with FA or with a mixture of FA and Cs without changing the principal thin-film deposition process within the series. Thus, we have ensured high data consistency as well as comparability of the crystal data and thin film properties. Henceforth, we refer to the compositions according to their A-site cation concentration in percent without subscript, e.g., Cs5FA5MA90 refers to Cs<sub>0.05</sub>FA<sub>0.05</sub>MA<sub>0.90</sub>PbI<sub>3</sub>. The perovskite thin films were deposited onto glass/indium tin oxide (ITO)/poly[bis(4-phenyl)(2,4,6-trimethylphenyl)amine] (PTAA) samples—a commonly used layer sequence for perovskite solar cells. The perovskite layer itself was deposited from mixtures of methylammonium iodide, formamidinium iodide, cesium iodide, lead iodide, and thiourea in N,N-dimethylformamide (DMF): N-methyl-2-pyrrolidone (NMP).<sup>[30–32]</sup> In our structure investigations, we omitted the top electrode and the electron transport layer for accessibility of the perovskite layer. For X-ray diffraction, we also omitted ITO to avoid additional reflections.

### 2.1. Tetragonal-To-Cubic Phase Transitions

An important prerequisite for the occurrence of ferroelectricity is a noncentrosymmetric space group. Phase-pure MAPbI<sub>3</sub> was reported to exhibit a tetragonal crystal phase at room temperature.<sup>[33]</sup> Toward elevated temperatures beyond the Curie temperature (*T*<sub>C</sub>), MAPbI<sub>3</sub> transitions into its cubic phase.<sup>[34]</sup> To investigate how the crystal phase changes upon gradual replacement of MA by FA and Cs, we conducted X-ray diffraction experiments in Bragg–Brentano geometry. In tetragonal MAPbI<sub>3</sub>, the PbI<sub>6</sub> octahedra are tilted.<sup>[33]</sup> Under copper K-α radiation, this ordered distortion produces a superlattice reflection at 2θ = 23.5° in the X-ray diffraction patterns. Notably, copper K-α radiation consists of K-α1 and K-α2 lines, which lead to splitting of the reflection.<sup>[35]</sup>

In **Figure 1**, the X-ray diffraction patterns of the FAMA and CsFAMA series are depicted, where MA was gradually replaced with FA. At MA concentrations ≥90%, we observe superlattice reflections due to octahedral tilting, whereas the diffraction patterns of the compositions with MA concentrations ≤85% exhibit no superlattice reflections and, hence, no octahedral tilting. With the octahedral tilting being indicative of the tetragonal phase, the structures transition from the tetragonal to the cubic phase at MA concentrations between 85% and 90%. This cross-over between the phases can shift toward higher or lower MA concentrations depending on the actual sample temperature, which is difficult to control with high precision in these and all following experiments. Toward lower MA concentrations, the *T*<sub>C</sub> is reduced, and, thus, samples may transition to the cubic phase at slightly elevated ambient temperatures. For example, Francisco-López et al. and Weber et al. reported tetragonal-to-cubic phase transition temperatures of FA10MA90 between 30 and 40 °C.<sup>[28,29]</sup> Accordingly, in a different set of measurements on hot summer days, we observed no superlattice reflection of FA10 MA90. Thus, we conclude a tetragonal-to-cubic phase transition when decreasing the MA concentration, in this experiment, in the realm of 85–90%.

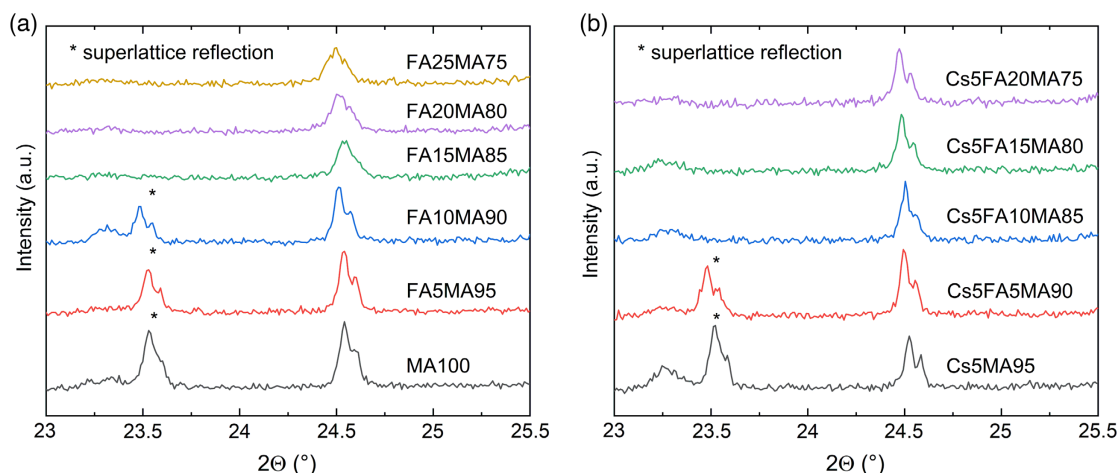


**Figure 1.** X-ray diffraction patterns of a) the FAMA series and b) the CsFAMA series were measured in Bragg–Brentano geometry with copper K- $\alpha$  radiation. Up to an MA concentration of 90%, the superlattice reflection (\*) induced by octahedral tilting occurs at  $2\theta = 23.5^\circ$ . At an MA concentration of 85% or less, the superlattice reflection vanishes.

## 2.2. Structural Analysis of CsFAMA Mixed-Cation Perovskites by Synchrotron X-ray Diffraction

The literature lacks crystallographic data on CsFAMA thin films with high MA concentrations. Thus, we employed more elaborate synchrotron X-ray diffraction measurements with a 2D detector. In these measurements, a sample orientation of  $90^\circ$  is equivalent to measurements in the Bragg–Brentano setup. We performed data analysis with the Strain, Texture, and Rietveld Analysis for Piezoceramics (STRAP) method, which enables the determination of a detailed structural model together with texture information.<sup>[36]</sup> A comparison of typical refinements and the corresponding background corrected data is shown in

**Figure 2.** Both refinements reveal a significant amount of secondary lead iodide phase, which stems from the excess lead iodide in the precursor solution. Furthermore, a clear texturing of both the perovskite and the lead iodide is observed.

However, the degree of texturing changes with the MA concentration. **Figure 3a** shows the maxima of the pole figure densities  $f(hkl)$  in multiples of random distribution (MRD) of the perovskite phase. The dashed line indicates  $\text{MRD} = 1$ , which corresponds to a nontextured material. For Cs5MA95, high MRD of around 6 is observed. With decreasing MA concentration, the maximum MRD continuously reduces to between 2 and 3. Simultaneously, the perovskite phase loses its tetragonality.

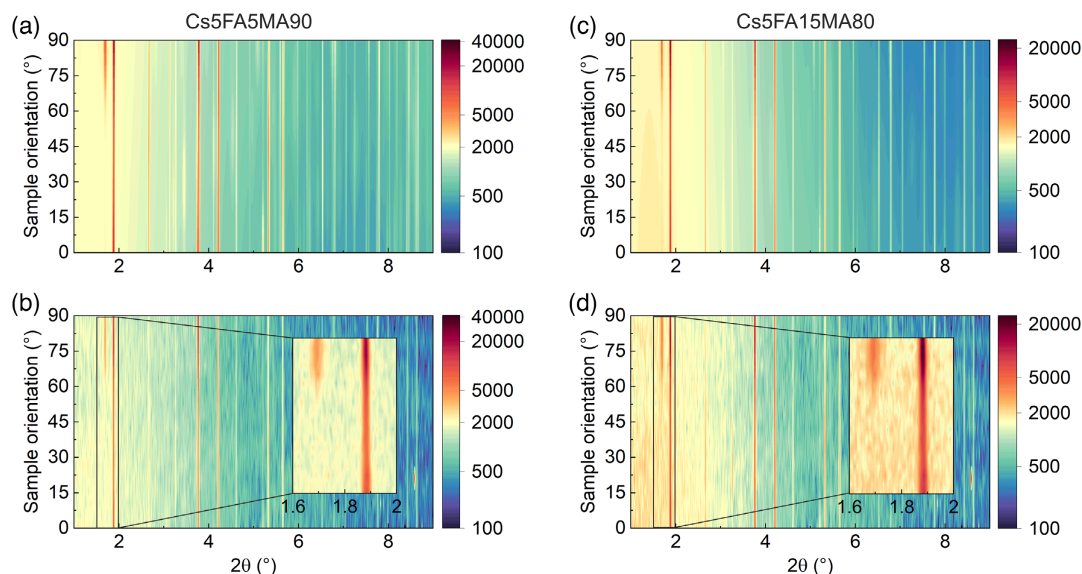


**Figure 2.** Rietveld refinement (top) and background corrected diffraction data (bottom) of a,b) Cs5FA5MA90, and c,d) Cs5FA15MA80 with the STRAP method. The insets show the sample orientation dependence of the 001 lead iodide reflection at  $2\theta = 1.7^\circ$  and the  $200_T/110_T/100_C$  perovskite reflection at  $2\theta = 1.9^\circ$ . Both phases are strongly textured. The intensities are plotted on a logarithmic scale for better visualization.

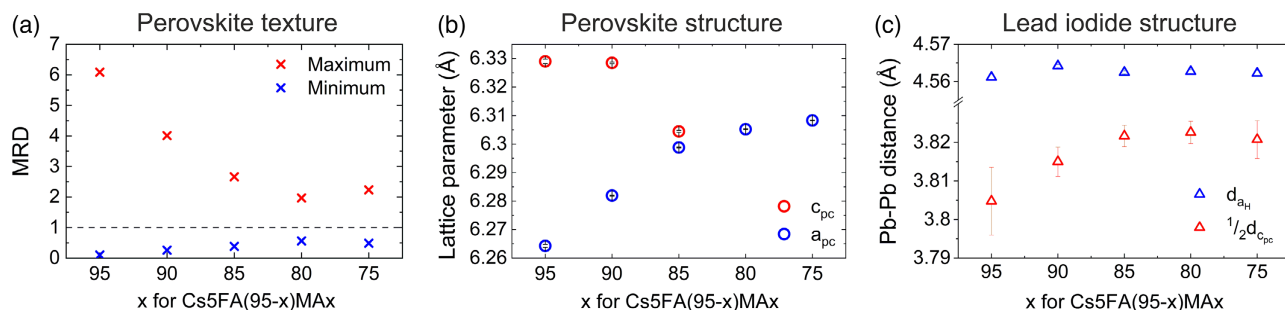


**Figure 3.** Refinement results from the texture analysis of Cs5FA(95-x)MAx (75 ≤ x ≤ 95). a) Texture extrema of the perovskite phase. b) Lattice parameters of the perovskite phase. c) Lattice parameters of the PbI<sub>2</sub> phase. For decreasing MA concentration, the texture becomes weaker and the tetragonality of the perovskite disappears. There is a correlation between the tetragonality of the perovskite phase and the lattice parameters of the PbI<sub>2</sub> phase.

This is reflected by the lattice parameters of the perovskite phase (Figure 3b). Here, the lattice parameters were recalculated to pseudocubic equivalents ( $a_{pc}$ ,  $c_{pc}$ ). For the tetragonal phase, these are defined as

$$a_{pc} = \frac{a_T}{\sqrt{2}} \text{ and } c_{pc} = \frac{c_T}{2} \quad (1)$$

The structure is clearly tetragonal with unit cell distortions  $\eta_T = 1.03(2)\%$  for Cs5MA95 and  $\eta_T = 0.741(7)\%$  for Cs5FA5MA90. Notably, while the c-axis vector of all tetragonal compositions has equal length, the length of the a-axis vector continuously increases toward lower MA concentration, as shown in Figure 3b. Cs5FA10MA85 marks the transition from tetragonal to pseudocubic. Here, the unit cell distortion is an order of magnitude smaller than for Cs5FA5MA90 and at the resolution limit of this diffraction experiment.

The compositions such as Cs5FA10MA85, Cs5FA15MA80, and Cs5FA20MA75 can all be refined with a cubic structure model. In this case, the diffraction patterns can be modeled with slight intensity deviations for the hhh reflections. Since these reflection intensities are dominated by the scattering of iodide ions, this indicates a remaining disorder of the octahedra. Local polar displacements by H-bonding, variations in cation displacements, or variations in cation distributions are possible explanations.

### 2.3. Relationship of the Lead Iodide and the Perovskite Structure

Even though the ordered unit cell distortion vanishes for Cs5FA10MA85–Cs5FA20MA75, the perovskite phase still shows significant texturing [ $f_{\max}(hkl) > 1$ ]. Since the perovskite thin film was deposited onto an amorphous PTAA layer on glass, there is no driving force toward the development of a 110<sub>T</sub> or 100<sub>C</sub> texture from the perovskite phase alone. However, the strong texture of the lead iodide phase may indicate a connection between the texture of lead iodide and the perovskite phase. To investigate the lead iodide structure and its relationship to the perovskite structure, we determined the distance of the Pb ions in the iodide octahedra. Lead iodide crystallizes in a layer structure with rhombohedral symmetry, where the iodide octahedra layers form in the  $a_H$ – $b_H$  plane. The subscript H denotes the hexagonal setting

of the rhombohedral unit cell. These layers exhibit an ABC stacking sequence along the  $c_H$ -axis, and the layers of iodide octahedra are separated by roughly twice the Pb–Pb distance in the  $a_H$ – $b_H$  plane. This layer structure explains the strong texture of lead iodide along the  $c_H$ -axis that was observed in the X-ray experiments (Figure 2). From the refined lattice parameters of the lead iodide phase, the distances of the iodide octahedra in the  $a_H$ – $b_H$  plane and along the  $c_H$ -axis can be calculated. The distance in the  $a_H$ – $b_H$  plane is the  $a_H$ -axis length and the distance along the  $c_H$ -axis can be expressed as the length of the pseudocubic c-axis

$$d_{c_{pc}} = \frac{\sqrt{4a_H^2 + c_H^2}}{6} \quad (2)$$

These Pb–Pb distances are shown in Figure 3c.  $d_{a_H}$  is constant for all compositions, which indicates that the individual lead iodide sheets are not affected by the FA modification. However, the stacking distance of the sheets, which is reflected by the Pb–Pb distance along the c-axis  $d_{c_{pc}}$ , constantly increases with increasing FA concentration. Lead iodide is known for its polytypism.<sup>[37]</sup> Hence, it seems plausible that a change in the chemical environment could alter the layer structure of lead iodide. Notably, the size of the PbI<sub>6</sub> octahedra in lead iodide is similar to their size in the perovskite phases and, especially, in Cs5MA95. The close relationship between the structures also becomes visible in STEM micrographs of MAPbI<sub>3</sub> that show coherent interfaces between the lead iodide and perovskite phase.<sup>[38]</sup> Therefore, the texture of lead iodide intermediate phases from the precursor thin film might induce the texture of the perovskite, independent of polar displacements, unit cell distortions, or octahedral tilting.

### 2.4. Ferroelectricity in Mixed-Cation Perovskite Thin Films

The identification of the important tetragonal-to-cubic phase transitions in the FAMA and the CsFAMA series for MA concentrations between 85% and 90% provided the framework for more detailed investigations of the ferroelectric nature of the samples. Since earlier studies produced evidence that textured MA100 thin films form ferroelectric domains with a polarization that is predominantly oriented in-plane,<sup>[39,40]</sup> we opted for lateral PFM measurements (LPFM, detection of in-plane piezoresponse

via torsion of the cantilever) using the bottom ITO layer as the counter electrode. For signal amplification, we applied an excitation frequency of a few kHz below the lateral contact resonance of the cantilever-sample system (250 kHz, Bruker SCM-PIC-V2) and used a moderate driving amplitude of 2 V. Notably, changes in the topography and, by extension, the stiffness of the cantilever-sample system can cause crosstalk by shifting the resonance frequency.<sup>[41]</sup> A comprehensive discussion on the applicability of PFM for probing ferroelectric domains in MAPbI<sub>3</sub> can be found elsewhere.<sup>[42]</sup>

The topographies, deflection errors, and LPFM quadratures of thin films of selected FAMA and CsFAMA compositions are shown in **Figure 4**. The first row shows the MAPbI<sub>3</sub> reference (MA100, Figure 4a–c), rows 2 and 3 show FAMA compositions (Figure 4d–i), and rows 4 and 5 show CsFAMA compositions (Figure 4j–o). According to the topography images (first column), the grain sizes of all compositions are comparable (up to 1 μm). The deflection error in the middle column helps identify grain boundaries that are less obvious in the actual topography image. As visible in the different height scales, the CsFAMA layers are slightly rougher than the FAMA layers, which we attribute to a subtle modification to the fabrication process: CsFAMA layers were exposed to solvent atmosphere under a petri dish, while the FAMA layers were dried with a nitrogen gun prior to thermal annealing. The magnitude of the scan deflection error (second column) is consistent across all samples, and topographical ridges are present in all thin-film compositions. In addition, some smaller features are present, which may be perovskite grains, residual lead iodide precursor, or complexes of lead iodide and thiourea. Residual lead iodide originates from the lead iodide excess used during fabrication. The presence of complexed thiourea is evidenced by the stretching vibrations of the sulfur carbon bond at 1398 cm<sup>-1</sup> in attenuated total reflectance-Fourier transform infrared spectroscopy (ATR-FTIR) (Figure S1, Supporting Information).<sup>[43]</sup> Both ridges and grain boundaries in all samples produce crosstalk between topography and LPFM signals and must not be misinterpreted for piezoresponse contrast or domain walls. Yet, ordered stripes of ferroelectric domains are clearly visible in LPFM as shown in Figure 4c and overlay topography features, which is well in accordance with earlier reports on MA100.<sup>[10,39,40]</sup> To maximize the visibility of these domains in the presence of topographic crosstalk, we discuss the quadrature of the LPFM signal, which is the product of the amplitude and the sine of the phase. Although the phase is rather noisy across large parts of the sample under investigation, domain walls show some contrast, which assists in the identification of domains (Figure S2, Supporting Information). Notably, we have demonstrated a clear 180° phase contrast between neighboring domains in MAPbI<sub>3</sub> before.<sup>[10]</sup> We attribute this discrepancy in phase contrast to the rough surface, which interferes with the LPFM measurement.

Strikingly, LPFM features (stripes) that are independent of the topography and the deflection error are only visible at MA concentrations ≥90% in both the FAMA and the CsFAMA series. In light of the known properties of MA100, we interpret these features as ferroelectric domains. Samples with MA concentrations ≤85% do not show any ferroelectric domain contrast, but only the ridges and grain boundaries that are also visible in the topography (Figure 4, S3, and S4, Supporting Information). These

LPFM measurements are well in accordance with the X-ray diffraction measurements above. Again, we observe a phase transition from the (tetragonal) ferroelectric phase to the (cubic) nonferroelectric phase in the realm of a MA concentration of 85–90%.

## 2.5. Correlation of Microstructure and Solar Cell Performance

Only the FAMA and CsFAMA compositions with high MA concentration are tetragonal and show ferroelectric domains in PFM. The FAMA and CsFAMA series provided a set of perovskite thin films around the composition-induced tetragonal-to-cubic phase transition regime to correlate the presence of ferroelectric domains with the solar cell performance experimentally. To obtain functional solar cells, the layer stack was completed with [6,6]-phenyl-C<sub>61</sub>-butyric acid methyl ester (PC<sub>61</sub>BM), bathocuproine (BCP), and silver. The gradual decrease of the bandgap energy for increasing FA concentration enables further absorption into the near-infrared, which is reflected in the redshift of the external quantum efficiency (EQE) onset by 10–15 nm (Figure S5 and S6, Supporting Information).

**Figure 5** shows the short-circuit current density ( $J_{SC}$ ), open-circuit voltage ( $V_{OC}$ ), fill factor (FF), and power conversion efficiency (PCE), which were obtained through  $J$ - $V$  scans of solar cells from the FAMA series under solar simulator illumination. PCE and  $J_{SC}$  were corrected using individual spectral mismatch factors for each composition (Figure S7, Table S8, Supporting Information). Since perovskite solar cells are known for their  $J$ - $V$  scan hysteresis, we differentiate between the descending scan, where the voltage is swept from the forward to the reverse direction, and the ascending scan, where the voltage is swept from the reverse to the forward direction (both at 300 mV s<sup>-1</sup>). As trends are similar in both cases, we only depict the performance data of solar cells extracted from the descending scan as shown in Figure 5. The results of the ascending scan are shown in Figure S9, Supporting Information. In addition, we measured all  $J$ - $V$  curves twice. The blue and green symbols represent the first and the second measurements, respectively.

For increasing FA (decreasing MA) concentration, we observe a gradual decrease in all solar cell parameters. The most substantial loss occurs in  $J_{SC}$ . Supplementary EQE measurements with (Figure S5, Supporting Information) and without bias light (Figure S10, Supporting Information) reveal that charge carriers are generated in the layer, but for increasing FA concentration and stronger irradiance (higher charge carrier densities), a large portion of these charge carriers is lost to recombination. The loss in  $V_{OC}$  across the cation compositions is less severe. Here, in the first scan, we find a loss of 20–30 mV, which matches well the change in bandgap energy. However, degradation leads to substantially lower  $J_{SC}$  and  $V_{OC}$  in the second scan.

**Figure 6** shows CsFAMA solar cells, which were measured under the same conditions as the FAMA series (descending scan, ascending scan as shown in Figure S11, Supporting Information).  $V_{OC}$ , FF, and PCE follow a similar trend and we also observe increased degradation for higher FA concentration. Direct comparison between the CsFAMA solar cells and the FAMA series at the same MA concentration shows an enhanced

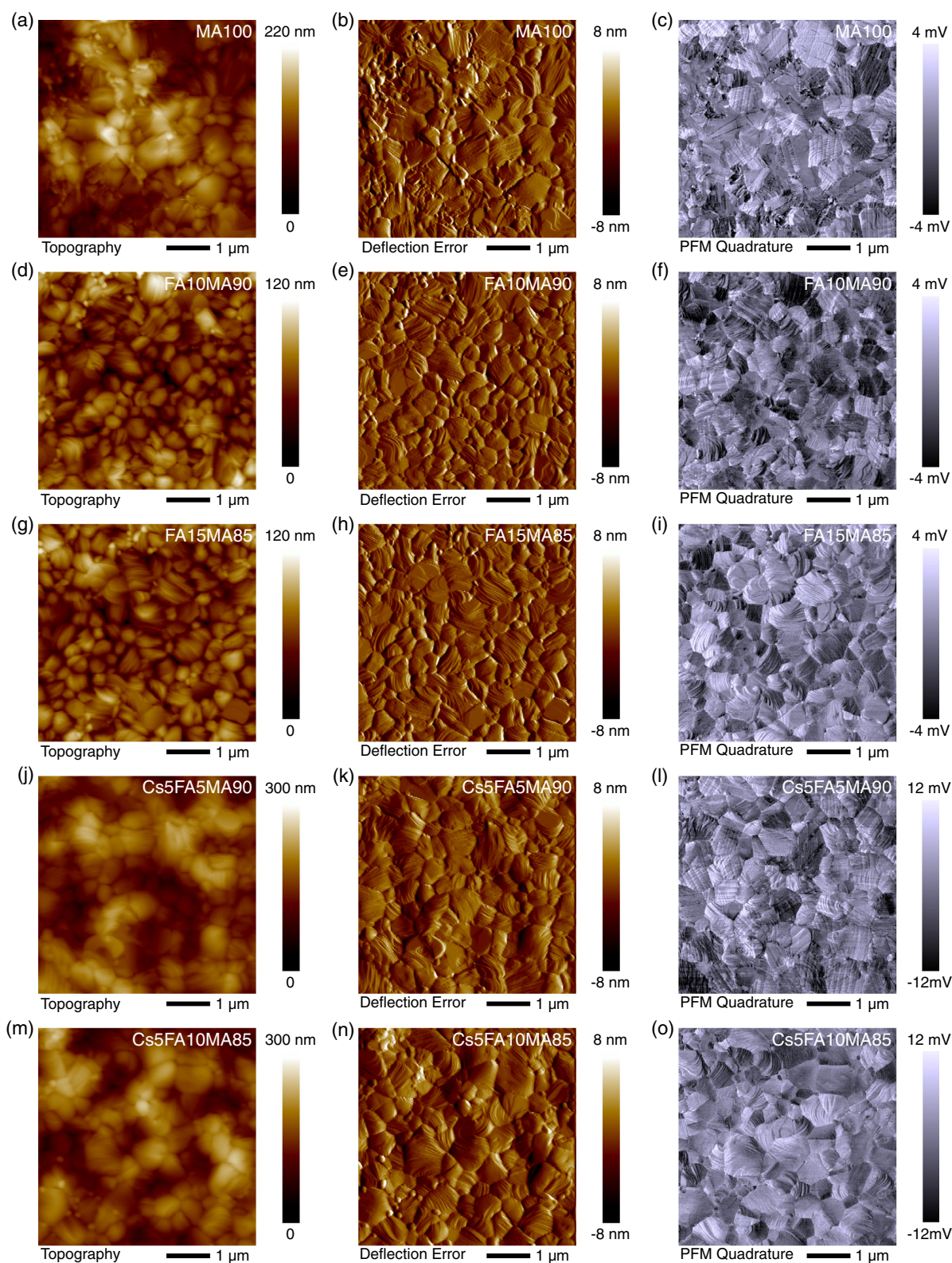


**Figure 4.** The five rows show thin films of five selected perovskite compositions with different Cs, FA, and MA concentration ( $5 \times 5 \mu\text{m}^2$ ). Left column: topography, center column: deflection error, and right column: LPFM quadrature. The quadrature of thin films with an MA concentration  $\geq 90\%$  exhibits ferroelectric domains (c,f,l), while no domains are visible at an MA concentration  $\leq 85\%$  (i,o). The structures visible in (i,o) only correlate to the respective sample topography and deflection error (g,h,m,n).

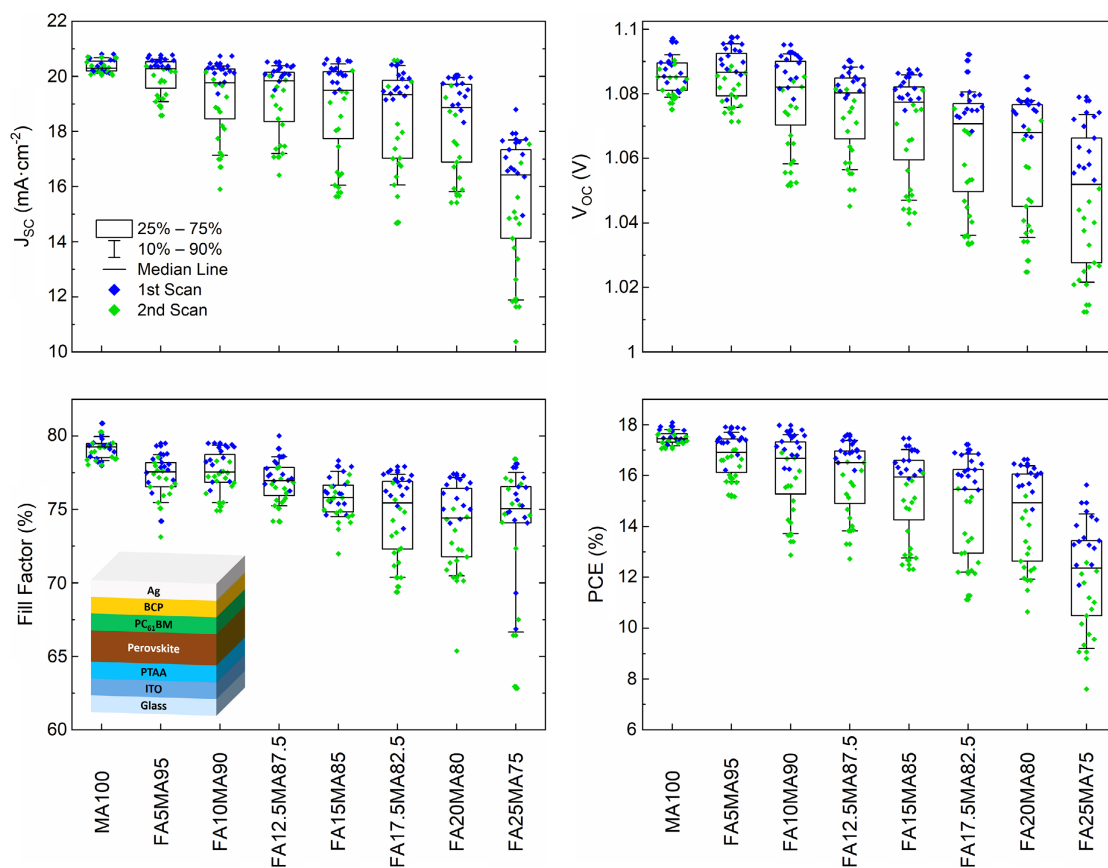


**Figure 5.**  $J_{sc}$ ,  $V_{oc}$ , FF, and PCE of FAMA solar cells (descending scan) versus decreasing MA (increasing FA) concentration. The solar cell performance reduces for smaller MA concentration and the difference between first and second measurements becomes larger. Statistics include 15–16 samples per composition (total yield: 126/128).

stability against degradation (1st vs. 2nd scan) for samples containing cesium.

So, in light of these results, does ferroelectricity enhance the device performance? Sherkar et al. and Rossi et al. predicted that ferroelectric in-plane polarization in a solar cell should primarily improve the fill factor.<sup>[4,5]</sup> Indeed, we observed some gradual improvement of the FF for light-harvesting layers with higher MA concentration that exhibits ferroelectric domains. Notably, the lattice parameters obtained from synchrotron X-ray diffraction (Figure 3b) are consistent with a continuous phase transition. Therefore, we expect a gradual change in polarization, which was also observed in other ferroelectrics.<sup>[44,45]</sup> In our experiments, the median FFs for MA100 were 79% (FAMA series) and 80% (CsFAMA series). FA20MA80, FA25MA75, Cs5FA15MA80, and Cs5FA20MA75 had median fill factors of 74%, 75%, 77%, and 75%, respectively. Yet, this improvement was not as pronounced as in the idealized simulations (FF of 84% to 69% for  $P = 0.05 \mu\text{C cm}^{-2}$  to  $P = 0$ ; FF of 77% to 52% for  $P = 0.4 \mu\text{C cm}^{-2}$  to  $P = 0$ ),<sup>[4,5]</sup> and the FF continued to decrease in the cubic regime. Unsurprisingly, to describe real devices quantitatively, other effects than ferroelectric polarization must be accounted for too. Such effects may include, for example, planar stacking defects as observed by Li et al. in FAMA solid solutions.<sup>[16]</sup> We point out that the series analyzed here was

fabricated for high process consistency and analytical comparability. For best solar cell efficiencies at every material composition, the fabrication would have to be optimized separately. Thus, while our devices perform best at MA100, other studies found highest power conversion efficiencies at ratios of FA40MA60, FA30MA70, and FA10MA90.<sup>[46–49]</sup>

### 3. Conclusion

We investigated two series of mixed-cation lead iodide perovskites, namely,  $\text{FA}_{1-x}\text{MA}_x\text{PbI}_3$  (FAMA,  $0.75 \leq x \leq 1$ ) and  $\text{Cs}_{0.05}\text{FA}_{0.95-x}\text{MA}_x\text{PbI}_3$  (CsFAMA,  $0.75 \leq x \leq 0.95$ ), for their crystal structures by X-ray diffraction and their ferroelectric domain patterns by lateral PFM. While compositions with high MA concentration show tetragonal crystal structure, ferroelectric domain patterns, and superlattice reflections from tilted  $\text{PbI}_6$  octahedra, thin films of lower MA concentration are cubic and nonferroelectric. The two regimes crossover in the realm of MA concentrations of 85–90%.

Upon incorporation as light-harvesting layers into solar cells, we observed a gradual reduction of the FF from higher to lower MA concentrations. Due to the strong consistency of the fabrication processes, the correlation of the structural and the

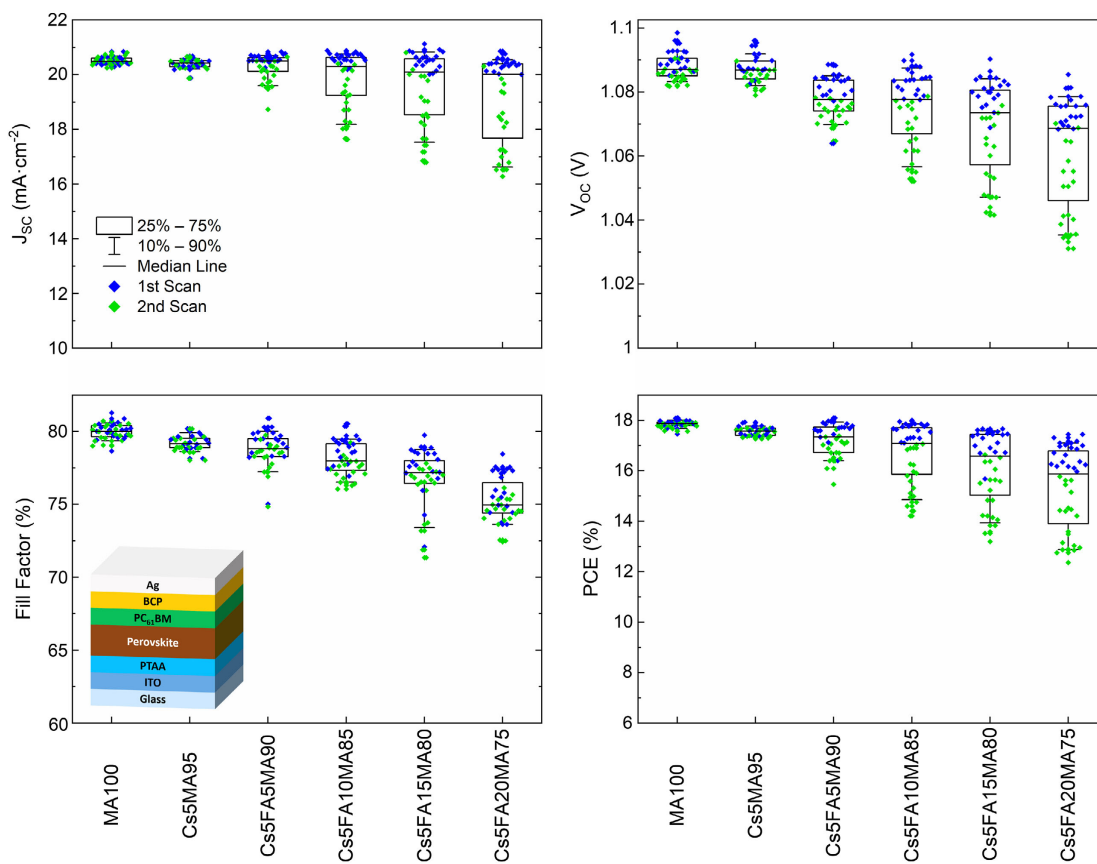


**Figure 6.**  $J_{sc}$ ,  $V_{oc}$ , FF, and PCE of CsFAMA solar cells (descending scan) versus increasing FA (decreasing MA) concentration. The solar cell performance decreases for smaller MA concentration and the difference between first and second measurements becomes larger. Statistics include 17–20 samples per composition (total yield: 117/120).

photovoltaic data suggests a positive influence of the ferroelectric material properties on the performance of solar cells. Yet, the magnitude of the effect in our real devices is smaller than predicted by earlier idealized simulations, and effects other than ferroelectric polarization are superimposed.

#### 4. Experimental Section

**Sample Preparation:** We used a modified version of the fabrication process by Brinkmann et al.<sup>[32]</sup> The solar cells were built with an ITO/PTAA/perovskite/PC<sub>61</sub>BM/BCP/Ag architecture with a photoactive area of  $3.5 \times 3.0 \text{ mm}^2$ . All substrates were cleaned in acetone and exposed to ultrasound (5 min). Afterward, they were rubbed with a glass cleaner-coated swab, rinsed with ethanol, and dried with a nitrogen gun. PTAA (Sigma-Aldrich) was dissolved in anhydrous toluene (99.8%, Sigma-Aldrich,  $1.25 \text{ g L}^{-1}$ ) and spin cast onto the samples (6000 rpm,  $1000 \text{ rpm s}^{-1}$ , 30 s, in air), followed by an oxygen plasma treatment (200 W, 40 kHz,  $0.5 \text{ NL h}^{-1}$ , 0.7 mbar, 1–2 s, and chamber volume: 10.5 L) to improve surface wetting.<sup>[50]</sup> All further deposition steps were carried out inside a glovebox under an inert N<sub>2</sub> atmosphere. The perovskite precursor solution was prepared by dissolving lead iodide (1.08 mmol, Alfa Aesar ultra dry) and a total of 1 mmol cesium iodide, methylammonium iodide, and/or formamidinium iodide per ml of DMF (99.8%, extra dry, Acros Organics): N-methyl-2-pyrrolidone (NMP) (99.5%, extra dry, Acros Organics). Thiourea (>99%, TCI) was added from a stock solution in DMF ( $100 \text{ g L}^{-1}$ ) to yield a final thiourea concentration of  $7.5 \text{ g L}^{-1}$  ( $0.1 \text{ mmol mL}^{-1}$ ) and a final DMF:NMP ratio of

1:1 by volume. After magnetic stirring at room temperature (>2 h), the solution was filtered with a polytetrafluoroethylene (PTFE) filter (pore size:  $0.2 \mu\text{m}$ ). For the perovskite deposition, a DMF:NMP atmosphere was created in the nitrogen-filled glovebox by spreading  $400 \mu\text{L}$  of DMF:NMP on a wipe. The precursor solution was then spin coated (3000 rpm,  $300 \text{ rpm s}^{-1}$ , 30 s). Immediately after spin coating, the samples were transferred to a vacuum chamber (volume: 5 L), which was evacuated for 60 s using a vacuum pump ( $12.7 \text{ m}^3 \text{ h}^{-1}$ , nominal final pressure: 0.007 mbar) and then refilled. To achieve high reproducibility of solar cells and smooth sample surfaces, samples were dried with a nitrogen gun (60 s) between vacuum exposure and thermal annealing ( $100^\circ\text{C}$ , 30 min). Then, all sources of solvent vapor were removed from the glovebox prior to two-stage spin coating ( $1000 \text{ rpm}$ ,  $1000 \text{ rpm s}^{-1}$ , 30 s;  $4000 \text{ rpm}$ ,  $1000 \text{ rpm s}^{-1}$ , 10 s) of a saturated and filtered ( $0.2 \mu\text{m}$ , PTFE) PC<sub>61</sub>BM (Lumtec) solution in anhydrous chlorobenzene (99.8%, Sigma-Aldrich). Fresh pipette tips were used for every sample. Next, BCP (Sigma-Aldrich) was spin coated ( $4000 \text{ rpm}$ ,  $2000 \text{ rpm s}^{-1}$ , 15 s) from ethanol solution ( $0.5 \text{ g L}^{-1}$ , <0.003% H<sub>2</sub>O, VWR). Solar cells were completed by evaporating silver in high vacuum ( $<3 \times 10^{-6}$  mbar, rate:  $1 \text{ \AA s}^{-1}$  up to a thickness of 10 nm and  $2 \text{ \AA s}^{-1}$  up to 100 nm).

**Piezoresponse Force Microscopy:** PFM samples were fabricated in the layer sequence described above, but omitting the PC<sub>61</sub>BM, BCP, and Ag top layers. The CsFAMA samples were exposed to an additional DMF:NMP solvent atmosphere under a petri dish after vacuum exposure and the nitrogen drying was omitted. All PFM measurements were carried out on a Bruker Dimension Icon atomic force microscope located inside a nitrogen-filled glovebox. We used Bruker SCM-PIC-V2 probes with a nominal tip radius of 25 nm and a nominal spring constant of  $0.1 \text{ N m}^{-1}$ . In this work, all samples within the FAMA series and all samples within the



CsFAMA series were measured with the same specific probe for best comparability. Notably, these results were also reproduced with other SCM-PIC-V2 probes. Scan rates of 0.5 Hz were used with 384 lines and 384 samples per line. The PFM drive frequency was 247.69 kHz for the FAMA series and 258.36 kHz for the CsFAMA series, in both cases a few kHz below the lateral resonance frequency. The PFM drive amplitude was 2 V. Multiple scans of the same area could be conducted at this voltage without any obvious sample degradation.

**X-ray Diffraction:** Perovskite layers for X-ray diffraction were deposited on glass/PTAA following the processes described above. Measurements in Bragg–Brentano geometry were performed with a Bruker D8 Advance (Bruker AXS) equipped with an energy discriminating LYNXEYE XE-T 1D detector using copper K- $\alpha$  radiation. Synchrotron X-ray diffraction experiments have been performed at the P02.1 beamline of PETRA III at the Deutsches Elektronen-Synchrotron (DESY).<sup>[51]</sup> Data were collected with a Perkin Elmer XRD 1621 detector at a wavelength of  $\lambda = 0.2073586(7)$  Å.<sup>[52]</sup> Texture was measured parallel to the perovskite film in a special geometry as reported elsewhere.<sup>[53]</sup> Data analysis was performed with the program MAUD with texture analysis as reported elsewhere.<sup>[36]</sup> During the first refinement, background parameters, scale factors, lattice parameters, and texture were refined. In addition, a general Debye–Waller factor for each phase and the atomic displacements of the tetragonal perovskite phase were refined.

**Solar Cell Characterization:** Solar cells were characterized under irradiation from a Scientech AX LightLine solar simulator (xenon arc lamp, AM1.5G filter). The solar simulator was calibrated using a monocrystalline silicon reference solar cell with a KG5 window (Newport 91150-KG5). Spectral mismatch factors were derived from spectral response measurements of the silicon reference solar cell and the perovskite solar cells (Figure S7, Supporting Information).<sup>[54]</sup> The spectral mismatch factors across the perovskite compositions range from 1.019 to 1.029 (Table S8, Supporting Information).  $J$ - $V$  curves were recorded on a source measure unit (SMU, Keithley 2400) at  $300 \text{ mV s}^{-1}$  in steps of 20 mV, starting with the descending scan from 1.4 to  $-0.4$  V, followed by the ascending scan from  $-0.4$  to 1.4 V. The current density as well as power conversion efficiency obtained from  $J$ - $V$  measurements was corrected for spectral mismatch.

## Supporting Information

Supporting Information is available from the Wiley Online Library or from the author.

## Acknowledgements

A.S., M.B., H.R., and A.C. acknowledge funding by the Carl Zeiss Foundation (project KeraSolar). H.R. and A.C. further appreciate funding by the Helmholtz Association (program Materials and Technologies for the Energy Transition). M.H. acknowledges the Deutsche Forschungsgemeinschaft for funding (grant number HI 1867/1-2) and the Fraunhofer Society for funding of the Attract group KoMatsu. The authors thank Martin Etter and Alexander Schoekel for beamtime support at the P02.1 beamline of DESY and Salma Begum, KIT, for the ATR-FTIR measurements.

Open Access funding enabled and organized by Projekt DEAL.

## Conflict of Interest

The authors declare no conflict of interest.

## Data Availability Statement

The data that support the findings of this study are available from the corresponding author upon reasonable request.

## Keywords

ferroelectricity, organic metal halides, perovskite solar cells, piezoresponse force microscopy, X-ray diffraction

Received: September 7, 2022

Revised: September 21, 2022

Published online:

- [1] J. M. Frost, K. T. Butler, F. Brivio, C. H. Hendon, M. van Schilfgaarde, A. Walsh, *Nano Lett.* **2014**, *14*, 2584.
- [2] S. Liu, F. Zheng, N. Z. Koocher, H. Takenaka, F. Wang, A. M. Rappe, *J. Phys. Chem. Lett.* **2015**, *6*, 693.
- [3] V. Sarritsu, N. Sestu, D. Marongiu, X. Chang, S. Masi, A. Rizzo, S. Colella, F. Quochi, M. Saba, A. Mura, G. Bongiovanni, *Sci. Rep.* **2017**, *7*, 44629.
- [4] D. Rossi, A. Pecchia, M. Auf der Maur, T. Leonhard, H. Röhm, M. J. Hoffmann, A. Colsmann, A. Di Carlo, *Nano Energy* **2018**, *48*, 20.
- [5] T. S. Sherkar, L. J. A. Koster, *Phys. Chem. Chem. Phys.* **2016**, *18*, 331.
- [6] Y. Kutes, L. Ye, Y. Zhou, S. Pang, B. D. Huey, N. P. Padture, *J. Phys. Chem. Lett.* **2014**, *5*, 3335.
- [7] I. M. Hermes, S. A. Bretschneider, V. W. Bergmann, D. Li, A. Klasen, J. Mars, W. Tremel, F. Laquai, H.-J. Butt, M. Mezger, R. Berger, B. J. Rodriguez, S. A. L. Weber, *J. Phys. Chem. C* **2016**, *120*, 5724.
- [8] H. Röhm, T. Leonhard, M. J. Hoffmann, A. Colsmann, *Energy Environ. Sci.* **2017**, *10*, 950.
- [9] E. Strelcov, Q. Dong, T. Li, J. Chae, Y. Shao, Y. Deng, A. Gruverman, J. Huang, A. Centrone, *Sci. Adv.* **2017**, *3*, e1602165.
- [10] H. Röhm, T. Leonhard, M. J. Hoffmann, A. Colsmann, *Adv. Funct. Mater.* **2020**, *30*, 1908657.
- [11] E. A. Little, *Phys. Rev.* **1955**, *98*, 978.
- [12] C. Kittel, *Solid State Commun.* **1972**, *10*, 119.
- [13] A. Amin, M. J. Haun, B. Badger, H. McKinstry, L. E. Cross, *Ferroelectrics* **1985**, *65*, 107.
- [14] Z. Yang, C.-C. Chueh, P.-W. Liang, M. Crump, F. Lin, Z. Zhu, A. K.-Y. Jen, *Nano Energy* **2016**, *22*, 328.
- [15] M. Saliba, T. Matsui, J.-Y. Seo, K. Domanski, J.-P. Correa-Baena, M. K. Nazeeruddin, S. M. Zakeeruddin, W. Tress, A. Abate, A. Hagfeldt, M. Grätzel, *Energy Environ. Sci.* **2016**, *9*, 1989.
- [16] W. Li, M. U. Rothmann, Y. Zhu, W. Chen, C. Yang, Y. Yuan, Y. Y. Choo, X. Wen, Y.-B. Cheng, U. Bach, J. Etheridge, *Nat. Energy* **2021**, *6*, 624.
- [17] K. Aizu, *Phys. Rev. B* **1970**, *2*, 754.
- [18] A. A. Bakulin, O. Selig, H. J. Bakker, Y. L. A. Rezus, C. Müller, T. Glaser, R. Lovrincic, Z. Sun, Z. Chen, A. Walsh, J. M. Frost, T. L. C. Jansen, *J. Phys. Chem. Lett.* **2015**, *6*, 3663.
- [19] J. M. Frost, A. Walsh, *Acc. Chem. Res.* **2016**, *49*, 528.
- [20] P. S. Whitfield, N. Herron, W. E. Guise, K. Page, Y. Q. Cheng, I. Milas, M. K. Crawford, *Sci. Rep.* **2016**, *6*, 35685.
- [21] V. C. A. Taylor, D. Tiwari, M. Duchi, P. M. Donaldson, I. P. Clark, D. J. Fermin, T. A. A. Oliver, *J. Phys. Chem. Lett.* **2018**, *9*, 895.
- [22] B. Yang, W. Ming, M.-H. Du, J. K. Keum, A. A. Puzetzy, C. M. Rouleau, J. Huang, D. B. Geohegan, X. Wang, K. Xiao, *Adv. Mater.* **2018**, *30*, 1705801.
- [23] J. Breternitz, F. Lehmann, S. A. Barnett, H. Nowell, S. Schorr, *Angew. Chem., Int. Ed.* **2020**, *59*, 424.
- [24] A. Stroppa, C. Quarti, F. De Angelis, S. Picozzi, *J. Phys. Chem. Lett.* **2015**, *6*, 2223.
- [25] M. T. Weller, O. J. Weber, J. M. Frost, A. Walsh, *J. Phys. Chem. Lett.* **2015**, *6*, 3209.
- [26] G. Kieslich, S. Sun, A. K. Cheetham, *Chem. Sci.* **2014**, *5*, 4712.
- [27] R. D. Shannon, *Acta Crystallogr.* **1976**, *32*, 751.

- [28] A. Francisco-López, B. Charles, M. I. Alonso, M. Garriga, M. Campoy-Quiles, M. T. Weller, A. R. Goñi, *J. Phys. Chem. C* **2020**, *124*, 3448.
- [29] O. J. Weber, B. Charles, M. T. Weller, *J. Mater. Chem. A* **2016**, *4*, 15375.
- [30] J.-W. Lee, H.-S. Kim, N.-G. Park, *Acc. Chem. Res.* **2016**, *49*, 311.
- [31] L. Gao, S. Huang, L. Chen, X. Li, B. Ding, S. Huang, G. Yang, *Sol. RRL* **2018**, *2*, 1800088.
- [32] K. O. Brinkmann, J. He, F. Schubert, J. Malerczyk, C. Kreusel, F. van gen Hassend, S. Weber, J. Song, J. Qu, T. Riedl, *ACS Appl. Mater. Interfaces* **2019**, *11*, 40172.
- [33] Y. Dang, Y. Liu, Y. Sun, D. Yuan, X. Liu, W. Lu, G. Liu, H. Xia, X. Tao, *CrystEngComm* **2015**, *17*, 665.
- [34] A. Poglitsch, D. Weber, *J. Chem. Phys.* **1987**, *87*, 6373.
- [35] M. H. Mendenhall, A. Henins, L. T. Hudson, C. I. Szabo, D. Windover, J. P. Cline, *J. Phys. B: At. Mol. Opt. Phys.* **2017**, *50*, 115004.
- [36] M. Hinterstein, K.-Y. Lee, S. Esslinger, J. Glaum, A. J. Studer, M. Hoffman, M. J. Hoffmann, *Phys. Rev. B* **2019**, *99*, 174107.
- [37] R. S. Mitchell, *Z. Kristallogr. – Cryst. Mater.* **1959**, *111*, 372.
- [38] M. U. Rothmann, J. S. Kim, J. Borchert, K. B. Lohmann, C. M. O'Leary, A. A. Sheader, L. Clark, H. J. Snaith, M. B. Johnston, P. D. Nellist, L. M. Herz, *Science* **2020**, *370*, eabb5940.
- [39] S. M. Vorpahl, R. Giridharagopal, G. E. Eperon, I. M. Hermes, S. A. L. Weber, D. S. Ginger, *ACS Appl. Energy Mater.* **2018**, *1*, 1534.
- [40] T. Leonhard, A. D. Schulz, H. Röhm, S. Wagner, F. J. Altermann, W. Rheinheimer, M. J. Hoffmann, A. Colmann, *Energy Technol.* **2019**, *7*, 1800989.
- [41] B. J. Rodriguez, C. Callahan, S. V. Kalinin, R. Proksch, *Nanotechnology* **2007**, *18*, 475504.
- [42] T. Leonhard, H. Röhm, A. D. Schulz, A. Colmann, in *Hybrid Perovskite Solar Cells: Characteristics and Operation* (Ed: H. Fujiwara), Wiley-VCH, Weinheim, Germany **2021**, Ch. 7.
- [43] K. Swaminathan, H. M. N. H. Irving, *J. Inorg. Nucl. Chem.* **1964**, *26*, 1291.
- [44] T. Qi, I. Grinberg, A. M. Rappe, *Phys. Rev. B* **2010**, *82*, 134113.
- [45] J. Chen, K. Nittala, J. S. Forrester, J. L. Jones, J. Deng, R. Yu, X. Xing, *J. Am. Chem. Soc.* **2011**, *133*, 11114.
- [46] M. Salado, L. Calio, R. Berger, S. Kazim, S. Ahmad, *Phys. Chem. Chem. Phys.* **2016**, *18*, 27148.
- [47] Y. Zhang, G. Grancini, Y. Feng, A. M. Asiri, M. K. Nazeeruddin, *ACS Energy Lett.* **2017**, *2*, 802.
- [48] Y. Zhao, X. Xu, H. Zhang, J. Shi, L. Zhu, H. Wu, D. Li, Y. Luo, Q. Meng, *J. Power Sources* **2017**, *359*, 147.
- [49] X. Guo, K. Ngai, M. Qin, X. Lu, J. Xu, M. Long, *Nanotechnology* **2020**, *32*, 075406.
- [50] S. Zhang, M. Stolterfoht, A. Armin, Q. Lin, F. Zu, J. Sobus, H. Jin, N. Koch, P. Meredith, P. L. Burn, D. Neher, *ACS Appl. Mater. Interfaces* **2018**, *10*, 21681.
- [51] A.-C. Dippel, H.-P. Liermann, J. T. Delitz, P. Walter, H. Schulte-Schrepping, O. H. Seeck, H. Franz, *J. Synchrotron Radiat.* **2015**, *22*, 675.
- [52] M. Herklotz, F. Scheiba, M. Hinterstein, K. Nikolowski, M. Knapp, A.-C. Dippel, L. Giebeler, J. Eckert, H. Ehrenberg, *J. Appl. Crystallogr.* **2013**, *46*, 1117.
- [53] K.-Y. Lee, X. Shi, N. Kumar, M. Hoffman, M. Etter, S. Checchia, J. Winter, L. Lemos da Silva, D. Seifert, M. Hinterstein, *Materials* **2020**, *13*, 1054.
- [54] C. H. Seaman, *Sol. Energy* **1982**, *29*, 291.